Bull Math Biol (2017) 79:209–235
DOI 10.1007/s11538-016-0233-6

Society for Mathematical Biology

ORIGINAL ARTICLE

A Multiscale Approach to the Migration of Cancer Stem Cells: Mathematical Modelling and Simulations

Nikolaos Sfakianakis[1] · **Niklas Kolbe**[1] · **Nadja Hellmann**[2] · **Mária Lukáčová-Medvid'ová**[1]

Received: 13 May 2016 / Accepted: 4 November 2016 / Published online: 30 November 2016

Abstract We propose a multiscale model for the invasion of the extracellular matrix by two types of cancer cells, the differentiated cancer cells and the cancer stem cells. We investigate the epithelial mesenchymal-like transition between them being driven primarily by the epidermal growth factors. We moreover take into account the transdifferentiation program of the cancer stem cells towards the cancer-associated fibroblast cells as well as the fibroblast-driven remodelling of the extracellular matrix. The proposed haptotaxis model combines the macroscopic phenomenon of the invasion of the extracellular matrix by both types of cancer cells with the microscopic dynamics of the epidermal growth factors. We analyse our model in a component-wise manner and compare our findings with the literature. We investigate pathological situations regarding the epidermal growth factors and accordingly propose "mathematical-treatment" scenarios to control the aggressiveness of the tumour.

Keywords Cancer stem cell invasion · Extracellular matrix · Epidermal growth factor receptors · Epithelial mesenchymal transition

✉ Nikolaos Sfakianakis
sfakiana@uni-mainz.de

Niklas Kolbe
kolbe@uni-mainz.de

Nadja Hellmann
nhellman@uni-mainz.de

Mária Lukáčová-Medvid'ová
lukacova@uni-mainz.de

[1] Institute of Mathematics, Johannes Gutenberg-University, Mainz, Germany

[2] Institute of Molecular Biophysics, Johannes Gutenberg-University, Mainz, Germany

1 Introduction

The mathematical study of cancer processes has been an active field of research since the 1950s (see, e.g. Nordling 1953; Armitage and Doll 1954; Fisher 1958). It covers a wide range of biological/bio-chemical processes of the tumour, from the perspective of modelling, analysis, and numerical simulations (see, e.g. Preziosi 2003; Perumpanani et al. 1996; Chaplain and Lolas 2005; Anderson et al. 2000; Gerisch and Chaplain 2008; Ganguly and Puri 2006; Michor 2008; Stiehl and Marciniak-Czochra 2012; Neagu et al. 2010; Johnston et al. 2010; Vainstein et al. 2012; Gupta et al. 2009).

The nature of the cancer cells has been under scientific scrutiny. A particular phenomenon, that interests us also in this paper, is the following: Although cancer cells exhibit higher proliferation rates than normal cells, recent evidence have revealed the existence of a subpopulation of the tumour that proliferates with lower rates and exhibits stem-like properties. In particular, they possess the abilities of self-renewal and cell differentiation, and can conditionally metastasize, i.e. they can detach from the primary tumour, invade the vascular system, and afflict secondary sites (Brabletz et al. 2005; Mani et al. 2008). These cancer cells, termed cancer stem cells (CSCs), constitute only a minor part of the tumour, while its bulk is comprised by the more proliferative and non-metastatic differentiated cancer cells (DCCs) (Thiery 2002; Reya et al. 2001). The CSCs were first demonstrated in human acute myeloid leukaemia and several solid tumours, such as breast, brain, melanoma, prostate, ovarian, and pancreatic (see Fan et al. 2013) and the references therein.

It is not completely known, where the CSCs originate from; a current theory supports that they emanate from the more usual DCCs after a de-differentiation program has taken place (Jordan et al. 2006; Gupta et al. 2009; Reya et al. 2001). This type of transition of cancer cells, influences their cellular potency and is related to the epithelial–mesenchymal transition (EMT), a type of cellular de-differentiation program that can also be found in normal tissue (Mani et al. 2008). After EMT, the newly sprout CSCs take the first step in the process of metastasis and invade the extracellular matrix (ECM), this is considered as one of the "hallmarks of cancer" (cf. Kong et al. 2011; Thiery 2002; Katsumo et al. 2013).

The EMT is triggered by components of the micro-environment of the tumour (Radisky 2005). A prime role in this mechanism is played by the epidermal growth factors (EGF) that stimulate cell growth, proliferation, and differentiation by binding to the corresponding cellular receptor EGFR (Voon et al. 2013; Shien et al. 2013).

This process can be briefly described as follows: The binding of an EGF molecule onto an EGFR stimulates ligand-induced dimerization that activates the protein-tyrosine kinase activity of the receptor which in turn initiates a signal cascade that results in a variety of changes within the cell leading to DNA synthesis. In certain pathological mutations, the activity of the tyrosine kinase is stuck in the "on" position and causes unregulated cell growth, untimely EMT, and over-expression of EGFRs (see also Sasaki et al. 2013; Mendelsohn and Baselga 2000) for a thorough description.

Over-expressed EGFRs are found in many types of tumours, including breast, thyroid, ovarian, colon, head, neck, and brain. In addition, EGFR over-expression has been linked to a poor prognosis in breast cancer and may promote proliferation, migration, invasion, and cell survival as well as inhibition of cell apoptosis (Gao et al. 2012).

The role of EGFR as oncogene (Kawamoto et al. 1984) has led to the development of anticancer therapies targeted against the EGFRs, the so-called EGFR inhibitors, that promise improved treatment for many types of solid tumours.

In this work, we consider a special type of taxis, namely the haptotaxis, in order to model the invasion of the ECM by the DCCs and CSCs. Haptotaxis describes the biased random motion along directions of either extracellular adhesion sites, or of the ECM-bound chemoattractants, or along their gradients. Haptotaxis is typically modelled under the paradigm of the Keller–Segel (KS) systems.[1] Since their initial derivation, KS systems have been successfully applied in a wide range of biological phenomena spanning from bacterial aggregations to wound healing and cancer modelling. In the modelling of cancer growth in particular, the Keller–Segel-type systems were extended to include enzymatic interactions/reactions, yielding advection-reaction-diffusion (ARD) models, see for instance the generic haptotaxis system proposed in Anderson et al. (2000) that takes into account ECM degradation by matrix metalloproteinases (MMPs), or the chemo- hapto-taxis system proposed in Chaplain and Lolas (2005) that addresses the role of the enzyme plasmin.

Besides degradation, the ECM is also dynamically remodelled; this process is essential not only for the developmental progress of healthy tissue (wound healing, organ homeostasis, etc.), but also for the metastatic progression of cancer (Cox and Erler 2011). Specifically, the degradation of the "normal ECM" and its replacement by "tumour induced ECM" leads to altered physiological conditions more advantageous for the tumour (Kaplan et al. 2005; Erler and Weaver 2009). Main characteristic in this process is the increased expression of fibroblast cells which results from a trans-differentiation program of the CSCs (see, e.g. Katsumo et al. 2013) for more details.

Our main objective is to model the EMT transition of the DCCs to CSCs, triggered by the interaction with the EGF molecules found in the extracellular environment and the cellular EGF receptors. In more detail, we couple the microscopic dynamics of the EGF attachment/detachment to EGFRs with the macroscopic dynamics of the ECM invasion. We assume that the microscopic processes are much faster than the kinematic properties of the cells, including their invasion of the ECM. The overall process is limited by the availability of free EGF molecules and by the number of free EGFRs on the surfaces of the cells.

The ECM invasion model that we have developed is an ARD haptotaxis system that includes both the DCCs and the CSCs, their kinematic properties, and the EMT. It moreover includes the ECM on which the cancer cells adhere. We assume that the ECM is degraded by a class of matrix degenerating metalloproteinases (MMPs)—secreted by the cancer cells. The ECM is also constantly remodelled by fibroblast cells; which are assumed to emanate from the CSCs via a transdifferentiation program (Kaplan et al. 2005; Erler and Weaver 2009; Katsumo et al. 2013).

We study the dynamics of the derived model on one- and two-dimensional computational domains. The numerical treatment of such problems is challenging due to the inherent heterogeneous spatio-temporal dynamics and the merging/emerging clusters of cancer cells that the solutions develop, see, e.g. Fig. 2. Thus, we employ

[1] First introduced in Keller and Segel (1970) to describe the aggregations of slime mould.

a second-order finite volume method equipped with a third-order time integration scheme, developed particularly for the needs of this type of problems, see Sect. 3 and our previous works (Kolbe et al. 2016; Hellmann et al. 2016) for more details. In our investigation, we also include a sensitivity analysis of the model with respect to its parameters. In particular, we investigate the effect that the parameters have on the mass of the tumour and on the invasiveness of the DCCs and CSCs.

Similar ECM invasion systems that account for non-homogeneous cancer cell populations and the transition between them exist in the literature (see, e.g. Andasari et al. 2011; Domschke et al. 2014; Stinner et al. 2015). However, in these works, a detailed investigation of the EMT-triggering mechanism is not included, rather it is assumed that EMT takes place with a constant rate. With our model, we can see the impact of pathological situations such as the depletion of EGF and identify significant differences in the production of CSCs between small and large tumours.

The rest of the paper is structured as follows: In Sect. 2, we derive the mathematical model. We do so in a subsystem-by-subsystem way and justify our choices in detail. In Sect. 3, we describe the numerical method we use to resolve our model, and the method employed in the parameter sensitivity analysis. In Sect. 4, we present and discuss a series of experiments aimed to highlight the influence of the various model components, to compare with existing results from the literature, and to deduce specific "mathematical-treatment" scenarios to control the aggressiveness of the CSCs.

2 Model

Our mathematical model is deterministic and phenomenological. The unknown variables represent densities of the corresponding model components. More precisely, we include the two types of cancer cells (DCCs and CSCs), the ECM, and the fibroblast cells that are responsible for the remodelling of the matrix, as well as matrix degenerating proteins. The model consists of three subsystems (a) the ECM invasion subsystem in which the basic components of the haptotaxis-driven motility of the cancer and fibroblast cells are included, (b) the EMT subsystem that is responsible for the EGF-driven transition of the CSCs to DCCs, and (c) the ECM remodelling subsystem which addresses the way that fibroblast cells reconstruct the ECM. In the paragraphs that follow, we present and justify each system separately, and at the end of this section, we concatenate them to derive the complete system.

2.1 The Cancer Invasion Subsystem

This part of the model is based on the original derivation of a chemotaxis systems by Keller and Segel (1970). Although these systems were initially developed to address the phenomenon of bacterial aggregation, they have been very successful in applications to a wide range of biological phenomena (see, e.g. Kurganov and Lukáčová-Medvid'ová 2014) and the references therein. In modelling cancer growth, KS-type systems have been adjusted to address haptotaxis and a large variety of interactions between the cancer cells and the extracellular environment (see, e.g. Alt and Lauffenburger 1987; Bellomo et al. 2008; Anderson et al. 2000).

For our model, we first employ the basic haptotactic system which features (a) the cellular diffusion and logistic proliferation of the cancer cells, (b) the proteolysis of the ECM by matrix degenerating metalloproteinases (MMPs), and (c) the chemical degradation, diffusion of the MMPs as well as their production by the cancer cells:

$$\begin{cases} \dfrac{\partial c}{\partial t} = D_c \Delta c - \chi \nabla \cdot (c \nabla v) + \mu c (1 - c - v)^+ \\ \dfrac{\partial v}{\partial t} = -\delta m v \\ \dfrac{\partial m}{\partial t} = D_m \Delta m + \alpha c - \beta m \end{cases}, \tag{1}$$

where the positive part function is defined as $(x)^+ = \max\{x, 0\}$. Here we denote the densities of the cancer cells, ECM, and MMPs by c, v, and m respectively.

A first assumption that we make in the model is that the cancer cells are "immortal"; we exclude hence any terms that describe age-dependent cell death. In a similar way, we exclude from the model cell death due to overcrowding and the competition for free space, so in effect, we consider the positive-part logistic proliferation as opposed to the more usual logistic proliferation. Note, moreover, that the system (1) and the ones that follow are presented in their scaled non-dimensional version. We provide information on the scaling coefficients and reference densities along with the parameter values in Table 1.

2.2 The EMT Subsystem

Both species of cancer cells invade the ECM in a similar way. Indeed, we assume that they both satisfy corresponding KS-type systems of the form (1). They are also coupled by the EMT, which works as a loss/gain term between them:

$$\begin{cases} \dfrac{\partial c^{\mathrm{D}}}{\partial t} = \text{diffusion} + \text{haptotaxis} - \mu_{\mathrm{EMT}}\, c^{\mathrm{D}} + \text{proliferation} \\ \dfrac{\partial c^{\mathrm{S}}}{\partial t} = \text{diffusion} + \text{haptotaxis} + \mu_{\mathrm{EMT}}\, c^{\mathrm{D}} + \text{proliferation} \end{cases}, \tag{2}$$

where by c^{D}, c^{S}, and μ_{EMT}, we denote the DCCs, CSCs, and EMT rate, respectively. As is typically done in the modelling of reaction between two components, we assume that the EMT depends on the amount of EGF—in particular on the occupied DCC-specific EGFRs—and on the local density of the DCCs. We assume moreover that the μ_{EMT} is an increasing function of the occupied EGFRs that stagnates asymptotically to a constant value, i.e.:

$$\mu_{\mathrm{EMT}} = \mu_0 \frac{[g]_b^{\mathrm{DCC}}}{\mu_{1/2} + [g]_b^{\mathrm{DCC}}}, \tag{3}$$

where $[g]_b^{\mathrm{DCC}}$ is the density of the EGF molecules that are bound onto the EGFRs, μ_0 is the maximum EMT rate, and $\mu_{1/2}$ is the critical amount of bound EGF $[g]_b^{\mathrm{DCC}}$

Table 1 Parameter values in their derived biological units and in a rescaled formulation which we have used in our simulations

Parameters		Bio. relevant value	Rescaled value	References
D_D	Diffusion coeff. of DCCs	$3.5 \times 10^{-10}\,\mathrm{cm}^2\,\mathrm{s}^{-1}$	3.5×10^{-4}	Bray (2001), Anderson et al. (2000), Chaplain and Lolas (2005)
D_S	Diffusion coeff. of CSCs	$3.8 \times 10^{-11}\,\mathrm{cm}^2\,\mathrm{s}^{-1}$	3.8×10^{-5}	Bray (2001), Andasari et al. (2011), our choice
D_F	Diffusion coeff. of fibroblasts	$3.5 \times 10^{-10}\,\mathrm{cm}^2\,\mathrm{s}^{-1}$	3.5×10^{-4}	Kim and Friedmann (2010), our choice
D_m	Diffusion coeff. of MMPs	$2.5 \times 10^{-9}\,\mathrm{cm}^2\,\mathrm{s}^{-1}$	2.5×10^{-3}	Robbins et al. (1965), Stokes et al. (1991), Chaplain and Lolas (2005)
χ_D	Haptotaxis coeff. of DCCs	$1.3\,\mathrm{cm}^{d+2}\mathrm{mol}^{-1}\,\mathrm{s}^{-1}$	8×10^{-3}	Stokes et al. (1991), Chaplain and Lolas (2005)
χ_S	Haptotaxis coeff. of CSCs	$62.5\,\mathrm{cm}^{d+2}\mathrm{mol}^{-1}\,\mathrm{s}^{-1}$	4×10^{-1}	Stokes et al. (1991), Andasari et al. (2011), our choice
χ_f	Haptotaxis coeff. of fibroblasts	$1.3\,\mathrm{cm}^{d+2}\mathrm{mol}^{-1}\,\mathrm{s}^{-1}$	8×10^{-3}	Stokes et al. (1991), our choice
λ^{D}	EGF receptors per DCC	1.9×10^7	1	Imai et al. (1982), Özcan et al. (2006), Klein et al. (2004), our choice
λ^{S}	EGF receptors per CSC	2.7×10^7	1.4	Imai et al. (1982), Özcan et al. (2006), Klein et al. (2004), our choice
k_D	EGF unbinding/binding	$3.2 \times 10^{-12}\,\mathrm{cm}^{-d}\mathrm{mol}$	2	Özcan et al. (2006), estimated
Γ	Average of total EGF	$8 \times 10^{-14}\,\mathrm{cm}^{-d}\mathrm{mol}$	0.05	Estimated
μ_0	EMT factor	$5.5 \times 10^{-6}\,\mathrm{s}^{-1}$	0.055	Estimated
$\mu_{1/2}$	Critical EGF density	$3.2 \times 10^{-12}\,\mathrm{cm}^{-d}\mathrm{mol}$	2	Estimated

Table 1 continued

Parameters		Bio. relevant value	Rescaled value	References
μ_D	Proliferation rate of DCCs	$2 \times 10^{-5}\,\mathrm{s}^{-1}$	0.2	Stokes and Lauffenburger (1991), Chaplain and Lolas (2005)
μ_S	Proliferation rate of CSCs	$10^{-5}\,\mathrm{s}^{-1}$	0.1	Our choice
μ_F	Proliferation rate of fibroblasts	$10^{-5}\,\mathrm{s}^{-1}$	0.1	Our choice
μ_v	ECM remodelling rate	$1.9 \times 10^{8}\,\mathrm{s}^{-1}$	25	Our choice
β_F	Apoptosis rate of fibroblasts	$3 \times 10^{-7}\,\mathrm{s}^{-1}$	3×10^{-3}	Kim and Friedmann (2010)
β_m	Decay rate of MMPs	$10^{-4}\,\mathrm{s}^{-1}$	1	Anderson et al. (2000)
α_D	MMP production rate of DCCs	$2.3\,\mathrm{s}^{-1}$	0.1	Anderson et al. (2000), Chaplain and Lolas (2005)
α_S	MMP production rate of CSCs	$22.9\,\mathrm{s}^{-1}$	1	Our choice
δ_v	ECM degradation rate	$5.3 \times 10^{9}\,\mathrm{cm}^{d}\,\mathrm{mol}^{-1}\mathrm{s}^{-1}$	1	Anderson et al. (2000), Chaplain and Lolas (2005)
μ_{TRA}	Transdifferentiation rate	$10^{-6}\,\mathrm{s}^{-1}$	0.01	Estimated
c^{ref}	Reference cell density	$8.3 \times 10^{-20}\,\mathrm{cm}^{-d}\,\mathrm{mol}$	–	Kim and Friedmann (2010)
v^{ref}	Reference ECM density	$6.4 \times 10^{-9}\,\mathrm{cm}^{-d}\,\mathrm{mol}$	–	Kim and Friedmann (2010)
m^{ref}	Reference MMP density	$1.9 \times 10^{-14}\,\mathrm{cm}^{-d}\,\mathrm{mol}$	–	Kim and Friedmann (2010)
g^{ref}	Reference EGF density	$1.6 \times 10^{-12}\,\mathrm{cm}^{-d}\,\mathrm{mol}$	–	Jeulin et al. (2008), Kim and Friedmann (2010)
D	Diffusion scaling coeff.	$10^{-6}\,\mathrm{cm}^{2}\mathrm{s}^{-1}$	–	Bray (2001), Chaplain and Lolas (2005)
t_{sc}	Time scaling coeff.	$10^{4}\,\mathrm{s}$	–	Anderson et al. (2000), Chaplain and Lolas (2005)

For the non-dimensionalization, the reference densities and the scaling coefficients in the lower part of the table have been used. The integer $d \in \{1, 2\}$ denotes the space dimension. Parameter values referenced by "our choice" have been chosen according to our biological understanding of the processes, while we have decided on "estimated" parameter values after numerical experimentation

needed to generate half of the maximum EMT rate μ_0. In effect, $\mu_{1/2}$ becomes the critical measure of EGF that characterizes the non-uniform EMT.

This modelling approach is quite general as it includes both the EGF and the DCCs densities. It has been motivated by similar previous approaches (i.e. Eladdadi and Isaacson 2008; Zhu et al. 2011) and was also employed by us in Hellmann et al. (2016). Although this choice of μ_{EMT} is a simplification of the biological reality, it suffices to exhibit the importance of considering a non-uniform EGF-driven EMT rate, see also Sect. 4.

In the rest of this section, we briefly describe the modelling/computation of μ_{EMT} and refer to Hellmann et al. (2016) for more details. We set $[g]_f$ to represent the amount of EGF that is free in the extracellular environment, $[g]_0$ the total (free and bound on both the DCCs and the CSCs) density of EGF. Accordingly, $[r]_0$, $[r]_b$, and $[r]_f$ denote the total, occupied, and free receptors on the surface of cancer cells. We assume that the EGF and EGFR are locally conserved:

$$[g]_0(t,x) = [g]_f(t,x) + [g]_b(t,x), \tag{4}$$

$$[r]_0(t,x) = [r]_f(t,x) + [r]_b(t,x), \tag{5}$$

for every $t \geq 0$ and $x \in \Omega \subset \mathbb{R}^d$ bounded, $d = 1, 2$. The binding/release of EGF to/from the EGFR receptors takes place with rates k_+/k_- and is the same for both the DCCs and the CSCs (see also Zhu et al. 2011). Moreover, we assume that the free EGF molecules diffuse in the extracellular environment:

$$\begin{cases} \partial_\tau [g]_b = k_+ [g]_f [r]_f - k_- [g]_b \\ \partial_\tau [g]_f = D_f \Delta [g]_f - k_+ [g]_f [r]_f + k_- [g]_b \end{cases}, \tag{6}$$

The dynamics in (6) take place during a microscopic time scale τ, which is related to the macroscopic time t through:

$$\tau(t) = \frac{t}{\varepsilon}, \quad 0 < \varepsilon \ll 1. \tag{7}$$

We express by $\big(g_b(t,x),\ g_f(t,x)\big) = \big([g]_b(\tau(t),x),\ [g]_f(\tau(t),x)\big)$ the variables of the parabolic system (6) in the t timescale and recall (5), to write the amount of free receptors as

$$[r]_f \ = \ [r]_0 - [r]_b \ = \ \lambda^{\text{S}} c^{\text{S}} + \lambda^{\text{D}} c^{\text{D}} - [g]_b,$$

where $\lambda^{\text{S}}, \lambda^{\text{D}}$ represent the average (free and bound) EGFR receptors per cell. We have assumed that every EGF receptor can be occupied by a single EGF molecule, i.e. $[r]_b = [g]_b$. We can now deduce from (6), after taking the formal limit as $\varepsilon \to 0$ in (7), the elliptic system:

$$\begin{cases} \dfrac{1}{k_D}\, g_f \left(\lambda^{\text{S}} c^{\text{S}} + \lambda^{\text{D}} c^{\text{D}} - g_b\right) - g_b = 0 \\ \Delta g_f = 0 \end{cases}, \tag{8}$$

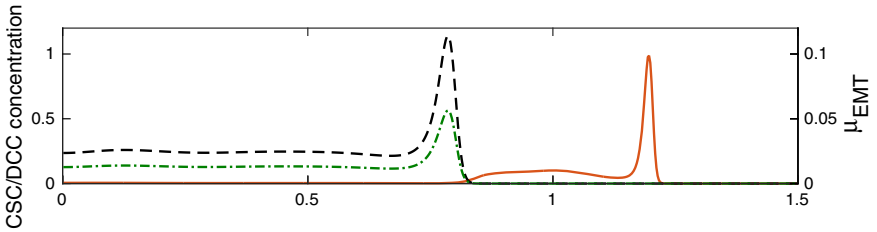

Fig. 1 Coefficient μ_{EMT} depends non-uniformly on the space variable x (here one-dimensional). This follows from the dependence of μ_{EMT} on c^{S} (13) which makes it also time-dependent, for more details (see Hellmann et al. 2016)

where $k_D = k_-/k_+$, the attachment/detachment ratio of the EGFs onto the EGFRs. The system (8) is also augmented with homogeneous Neumann boundary conditions,

$$\frac{\partial g_f(x)}{\partial \mathbf{n}} = 0, \quad x \in \partial\Omega\,. \tag{9}$$

where $\mathbf{n}$ is the outward unit normal vector to the computational domain of the equation (8). The uniqueness of the solution of (8)–(9) is recovered by the additional assumption that the total amount of EGF remains constant,

$$\Gamma = \frac{1}{|\Omega|}\int_\Omega g_0(t,x)\,\mathrm{d}x = \frac{1}{|\Omega|}\left(\int_\Omega g_b(t,x)\,\mathrm{d}x + \int_\Omega g_f(t,x)\,\mathrm{d}x\right). \tag{10}$$

With the above assumptions, the system (8) can be solved to give

$$g_b = \frac{g_f}{k_D + g_f}\left(\lambda^{\mathrm{S}} c^{\mathrm{S}} + \lambda^{\mathrm{D}} c^{\mathrm{D}}\right), \tag{11}$$

and in particular

$$g_b^{\mathrm{DCC}} = \frac{g_f}{k_D + g_f}\lambda^{\mathrm{D}} c^{\mathrm{D}}. \tag{12}$$

When combined with (3), we obtain

$$\mu_{\mathrm{EMT}} = \mu_0 \frac{g_f \lambda^{\mathrm{D}} c^{\mathrm{D}}}{\mu_{1/2} k_D + \mu_{1/2} g_f + g_f \lambda^{\mathrm{D}} c^{\mathrm{D}}}, \tag{13}$$

which is non-uniform in space and time, see also Fig. 1. On the other hand, the free EGF g_f is constant in space and is given by the unique positive root of the quadratic equation (see also Hellmann et al. 2016 for more details):

$$0 = g_f^2 + \left(k_D + \frac{1}{|\Omega|}\int_\Omega \lambda^{\mathrm{S}} c^{\mathrm{S}} + \lambda^{\mathrm{D}} c^{\mathrm{D}}\mathrm{d}x - \Gamma\right) g_f - \Gamma. \tag{14}$$

2.3 Fibroblast Cells and the Matrix Remodelling Subsystem

We describe the remodelling of the ECM with two subsystems. In the first, we introduce the transition/transdifferentiation of the CSCs to cancer-associated fibroblast cells, and in the second, we model the reconstruction of the ECM by the fibroblast cells. Contrary to the more usual assumptions of spontaneous or self-remodelling of the ECM, we promote in this work the more biologically relevant fibroblast-driven matrix remodelling.

The Transdifferentiation Subsystem The tumour environment is populated by fibroblasts which are locally enriched by a transdifferentiation programme of CSCs to cancer-associated fibroblast cells (Katsumo et al. 2013). In this work, we do not make a distinction between the two types of fibroblast cells, or the two types of induced ECM, although they present different biochemical and mechanical properties. We leave this question for a future investigation.

We assume that, similarly to the wound healing case, the fibroblast cells are directed towards regions of the ECM that need reconstruction. We model this property with a haptotactic movement towards lower densities of the ECM (Kim et al. 2009). This assumption is in a strong contrast to the haptotactic motion of the DCCs and CSCs, which is oriented towards the higher ECM densities.

For their proliferation, we employ the positive-part logistic function to account only for the competition for free space and neglect the overcrowding induced cell death. Since the fibroblast cells exhibit a much shorter life span than the "immortal" cancer cells, we include an apoptosis term with a constant rate. This is a simplified assumption but suffices for the needs of this work. Accordingly, the transdifferentiation subsystem reads as:

$$\begin{cases} \dfrac{\partial c^{\mathrm{S}}}{\partial t} = \text{diffusion} - \chi_S \nabla \cdot \left(c^{\mathrm{S}} \nabla v \right) - \mu_{\mathrm{TRA}}\, c^{\mathrm{CSC}} + \text{proliferation} \\ \dfrac{\partial c^{\mathrm{F}}}{\partial t} = \text{diffusion} + \chi_F \nabla \cdot \left(c^{\mathrm{F}} \nabla v \right) + \mu_{\mathrm{TRA}}\, c^{\mathrm{CSC}} \\ \qquad\qquad + \mu_F\, c^{\mathrm{F}} (1 - c^{\mathrm{D}} - c^{\mathrm{S}} - c^{\mathrm{F}} - v)^{+} - \beta_F\, c^{\mathrm{F}} \end{cases}, \tag{15}$$

where c^{F} represents the density of the fibroblast cells, χ_F their haptotactic sensitivity, μ_{TRA} their transdifferentiation production coefficient, and μ_F and β_F their proliferation and apoptosis/decay rate.

The Matrix Remodelling Subsystem Contrary to the more usual assumption of spontaneous or self-remodelling of the ECM, we promote here the (more biologically relevant) fibroblast-driven ECM remodelling limited by the availability of the free space and encoded by a logistic term:

$$\begin{cases} \dfrac{\partial c^{\mathrm{F}}}{\partial t} = \text{diffusion} + \text{haptotaxis} + \text{transdiff.} + \text{proliferation} \\ \dfrac{\partial v}{\partial t} = -\text{proteolysis} + \mu_F\, c^{\mathrm{F}} (1 - c^{\mathrm{D}} - c^{\mathrm{S}} - c^{\mathrm{F}} - v)^{+} \end{cases}, \tag{16}$$

where we again consider the positive-part logistic volume filling reaction term to account only for the remodelling of the matrix and not for its degradation. In fact, we assume that the matrix is degraded only by the proteolytic proteins MMP. The effect of the fibroblast-driven matrix remodelling in comparison with the more usual self-remodelling is shown in Fig. 4.

2.4 The Full Cancer Invasion System

In total, the complete ECM invasion model results from the concatenation of the subsystems (1), (2), (15), and (16) and reads as follows:

$$\begin{aligned}
\frac{\partial c^{\mathrm{D}}}{\partial t} &= D_D \Delta c^{\mathrm{D}} - \chi_D \nabla \cdot \left(c^{\mathrm{D}} \nabla v \right) - \mu_{\mathrm{EMT}}\, c^{\mathrm{D}} + \mu_D\, c^{\mathrm{D}} \left(1 - c^{\mathrm{D}} - c^{\mathrm{S}} - c^{\mathrm{F}} - v\right)^+, \\
\frac{\partial c^{\mathrm{S}}}{\partial t} &= D_S \Delta c^{\mathrm{S}} - \chi_S \nabla \cdot \left(c^{\mathrm{S}} \nabla v \right) - \mu_{\mathrm{TRA}}\, c^{\mathrm{S}} + \mu_{\mathrm{EMT}}\, c^{\mathrm{D}} \\
&\quad + \mu_S\, c^{\mathrm{S}} \left(1 - c^{\mathrm{D}} - c^{\mathrm{S}} - c^{\mathrm{F}} - v\right)^+, \\
\frac{\partial c^{\mathrm{F}}}{\partial t} &= D_F \Delta c^{\mathrm{F}} + \chi_F \nabla \cdot \left(c^{\mathrm{F}} \nabla v \right) + \mu_{\mathrm{TRA}}\, c^{\mathrm{S}} - \beta_F\, c^{\mathrm{F}} \\
&\quad + \mu_F\, c^{\mathrm{F}} \left(1 - c^{\mathrm{D}} - c^{\mathrm{S}} - c^{\mathrm{F}} - v\right)^+, \\
\frac{\partial v}{\partial t} &= -\delta_v\, m v + \mu_v\, c^{\mathrm{F}} \left(1 - c^{\mathrm{D}} - c^{\mathrm{S}} - c^{\mathrm{F}} - v\right)^+, \\
\frac{\partial m}{\partial t} &= D_m \Delta m + \alpha_D\, c^{\mathrm{D}} + \alpha_S\, c^{\mathrm{S}} - \beta_m\, m.
\end{aligned} \tag{17}$$

This system is complemented by appropriate initial conditions and no-flux boundary conditions:

$$-D_D \frac{\partial c^{\mathrm{D}}}{\partial \mathbf{n}} + \chi_D c^{\mathrm{D}} \frac{\partial v}{\partial \mathbf{n}} = -D_S \frac{\partial c^{\mathrm{S}}}{\partial \mathbf{n}} + \chi_S c^{\mathrm{S}} \frac{\partial v}{\partial \mathbf{n}} = \frac{\partial m}{\partial \mathbf{n}} = 0, \tag{18}$$

where $\mathbf{n}$ is the outward unit normal vector to the computational domain Ω. The model parameters are listed in Table 1. They follow from investigations in the literature (e.g. Kim and Friedmann 2010; Andasari et al. 2011; McDougall et al. 2002), and from our numerical experimentation and reflect the current biological understanding of the problem.

Further phenomena could also be included in the model. One such example is the orientation of the ECM fibres (see e.g. Hillen and Painter 2012; Hillen and Painter 2013), and the way they influence the invasion of the ECM and the EMT. Another example is the inclusion of EGFR inhibitors, which suppress the EMT, as is done in cancer therapy.

3 Mathematical Methods

In this section, we present two mathematical techniques that we apply in order to investigate the dynamical behaviour of (17) and (18) and to predict the evolution

of cancer cells. First, we briefly describe the main components of our higher-order implicit–explicit finite volume numerical scheme. In the second part, we explain the way we compute parameter sensitivities.

3.1 Numerical Method

It is well known that the solutions of the macroscopic cancer invasion systems typically develop clusters of cancer cell concentrations. The emerging of new clusters in time as well as their movement and interaction with each other makes the numerical treatment particularly challenging. The partial differential equation system (17) that we consider can be classified as an advection–diffusion–reaction system. A wealth of numerical methods for these kinds of systems in biological applications has been developed and studied (see, e.g. Hundsdorfer and Verwer 2003; Gerisch and Chaplain 2006; Kolbe et al. 2016; Kurganov and Lukáčová-Medvid'ová 2014).

For the numerical simulations in this work, we apply the finite volume method that we have developed previously in Kolbe et al. (2016). We first discretize in space to derive a system of ordinary differential equations

$$\frac{\partial \mathbf{w_h}}{\partial t} = \mathcal{A}(\mathbf{w_h}) + \mathcal{D}(\mathbf{w_h}) + \mathcal{R}(\mathbf{w_h}), \tag{19}$$

where $\mathbf{w_h}$ denotes a vector carrying the values of a piecewise constant function on N spatially uniform computational cells for all components of the system. In principle, non-uniform grids can also be used. As a matter of fact, in Kolbe et al. (2016), we have seen in one-dimensional settings the benefit of employing Adaptive Mesh Reconstruction (AMR) methods in terms of accuracy and efficiency. The application of AMR methods in two-dimensional setting will be the theme of a separate work.

The vector-valued operators $\mathcal{A}$, $\mathcal{D}$, and $\mathcal{R}$ approximate the advection (i.e. haptotaxis), diffusion, and reaction terms of the system for every computational cell and every component of a finite volume solution $\mathbf{w_h}$.

We choose the diffusion and reaction operators in a conventional way. Central differences approximate the second derivative in the diffusion operator $\mathcal{D}$, and reaction terms are directly evaluated at the cell centres in the reaction operator $\mathcal{R}$. In order to compute fluxes for haptotaxis in a given cell, we employ the dimensional splitting. Therefore, we address briefly the advection operator $\mathcal{A}$ only in one dimension. Let c_i be the density of a migrating cell type c (DCCs, CSCs, or fibroblasts) in the computational cell C_i and c_{i+1}, c_{i-1} the densities in the adjacent computational cells. We consider the approximation,

$$\int_{C_i} \chi \, \nabla \cdot (c \nabla v) \approx a_{i+1/2}\, c_{i+1/2} - a_{i-1/2}\, c_{i-1/2}, \tag{20}$$

where $a_{i\pm 1/2}$ refers to the characteristic velocities, and $c_{i\pm 1/2}$ to the reconstruction of cell densities at the interfaces of the computational cell.

The characteristic velocities in the haptotaxis case are proportional to the gradients of extracellular matrix density v. These are approximated by two-point

central differences. For the interface reconstructions, we compute slopes, using the minimized-central (MC) limiter (Leer 1977),

$$s_i = \text{minmod}\left(c_i - c_{i-1},\ \frac{1}{4}(c_{i+1} - c_{i-1}),\ c_{i+1} - c_i\right), \tag{21}$$

where

$$\text{minmod}(a, b, c) = \begin{cases} \min\{|a|, |b|, |c|\}\ \ \text{sign}(b), & \text{if a,b,c} > 0, \text{ or a, b, c} < 0, \\ 0, & \text{otherwise.} \end{cases}$$

Afterwards, we apply upwinding and define the reconstructed cell interfaces values

$$c_{i+1/2} = c_{i+1-1/2} = \begin{cases} c_i + s_i, & \text{if } a_{i+1/2} > 0, \\ c_{i+1} - s_{i+1}, & \text{otherwise.} \end{cases} \tag{22}$$

The resulting system of ODEs (19) is stiff due to the approximate diffusion operator. To reduce the number of time steps, which would be required by an explicit method, we employ implicit–explicit (IMEX) Runge Kutta schemes (Pareschi and Russo 2005; Kennedy and Carpenter 2003). The time integration scheme reads as follows

$$\begin{aligned} \mathbf{W_i} &= \mathbf{w_h^n} + \Delta t^n \sum_{j=1}^{i-1} a_{ij}^E\, (\mathcal{A} + \mathcal{R})(\mathbf{W_j}) + \Delta t^n \sum_{j=1}^{i} a_{ij}^I\, \mathcal{D}(\mathbf{W_j}), \\ i &= 1, \ldots, k+1, \quad \mathbf{w_h^{n+1}} = \mathbf{W_{k+1}}, \end{aligned} \tag{23}$$

thus, we apply an explicit Runge Kutta method (a_{ij}^E) to the advection and reaction terms coupled with a diagonally implicit method (a_{ij}^I) for the diffusion terms. The Butcher tableau we employ has been derived in Kennedy and Carpenter (2003), and it yields a four-stage scheme that is third-order accurate in time. The implicit treatment of diffusion allows us to use time steps Δt^n proportional to the diameter of the computational cells and the Courant–Friedrichs–Lewy stability number 0.49. Note that in the case of the system (17), our method is positivity preserving, i.e. given non-negative initial data, the numerical solution stays non-negative. We have already successfully applied this numerical method to study a chemotaxis–haptotaxis cancer system that promotes the role of urokinase in the invasion of the ECM, and a preliminary version of the model (17) (see Kolbe et al. 2016; Hellmann et al. 2016).

In Table 2, we demonstrate the second-order experimental order of convergence (EOC) of our numerical method in one- and two-space dimensions. To this end, we have consecutively refined the grid globally and compared the numerical solutions. The experimental order has been computed using the formula,

$$EOC(N) = \log_2(E(N)) - \log_2 E(N/2), \tag{24}$$

where $E(N)$ is the numerical error on a grid with N mesh cells in each space dimension. The second-order EOC confirms that the phenomena we exhibit in Sect. 4 are not numerical artefacts but are rather inherent properties of the mathematical model.

Table 2 Experimental convergence rates of the numerical method presented in Sect. 3.1 employed in the system (17) for the DCCs in one-dimensional (left) and two-dimensional (right)

Grid	L^1 error	EOC	L^2 error	EOC	Grid	L^1 error	EOC	L^2 error	EOC
512/1024	1.953e−05		3.199e−05		$16 \times 16/32 \times 32$	1.020e−01		3.025e−02	
1024/2048	4.430e−06	2.140	7.359e−06	2.120	$32 \times 32/64 \times 64$	3.090e−02	1.723	1.023e-02	1.564
2048/4096	1.061e−06	2.062	1.656e−06	2.152	$64 \times 64/128 \times 128$	8.453e−03	1.870	2.715e−03	1.914
4096/8192	2.569e−07	2.046	3.857e−07	2.102	$128 \times 128/256 \times 256$	2.180e−03	1.955	6.945e−04	1.967

In the one-dimensional case, Experiment Ia is performed for the final time $t = 15$, and in the two-dimensional case, Experiment IIId is realized for the final time $t = 10$. In both cases, the results confirm the second-order convergence of the numerical method

3.2 Parameter Study

In phenomenological models like (17), the dependence of the system dynamics on changes of the parameters is very interesting. Applying a local parameter analysis, we can deduce the influence that each part of the model has in the invasion process of the ECM by the cancer species. Accordingly, the parameters can be adjusted to better fit the model to realistic experimental data.

For this process, we recompute numerical solutions for the one-dimensional Experiment Ia, see Sect. 4, at the time instance $t = 15$, varying one parameter at a time and measure real-valued functionals $\mathcal{F}$ of the solution with respect to the parameter changes. We are particularly interested in the mass of the DCCs and CSCs over the whole domain Ω, the distance from the propagating CSC front to the slower DCC front, which quantifies the invasiveness of the CSCs, and the concentration of mesenchymal cells in the invading front.

For a more comprehensive overview of the influence of all model parameters, we have computed the parameter sensitivity of the aforementioned functionals. This means that we compute approximate derivatives of the functionals with respect to the parameters. Again, we consider here Experiment Ia at $t = 15$. For feasibility, we employ for each parameter p central differences around the corresponding value p_0 from Table 1 with a relative step size of $\delta p = p_0 \times 10^{-2}$ to compute the sensitivities

$$\mathcal{S}_p^{\mathcal{F}} = \frac{\mathcal{F}(\mathbf{w_h}^{t=15}(p = p_0 + \delta p)) - \mathcal{F}(\mathbf{w_h}^{t=15}(p = p_0 - \delta p))}{2\delta p} \approx \frac{\partial}{\partial p}\mathcal{F}(\mathbf{w_h}^{t=15}), \tag{25}$$

where $\mathcal{F}$ is the functional of interest, and $\mathbf{w_h}^{t=15}$ is the numerical solution (all components) of system (17), at time instance $t = 15$.

In Table 3, we present the results of this computation. Positive sensitivities $\mathcal{S}_p^{\mathcal{F}}$ indicate an increase in the functional $\mathcal{F}$ (in the corresponding column) when increasing the parameter p (in the corresponding line), while negative sensitivities indicate a decrease in the functional when increasing p. The absolute value quantifies the parameter influence on the corresponding attributes. Note that the sensitivity shows the effect, when increasing the parameter by one unit. Zero sensitivities in the column

Table 3 Sensitivity of model properties with respect to the model parameters in Experiment Ia

Parameters		DCC mass	CSC mass	Front distance	Front height
D_D	Diffusion coeff. of DCCs	+1.2342e+01	−8.1722e+00	+1.3714e+02	−7.3024e+01
D_S	Diffusion coeff. of CSCs	+9.4182e−02	−3.2915e−01	±0	−9.5376e+03
D_F	Diffusion coeff. of fibroblasts	−2.2642e−02	+2.1300e−03	±0	+3.9125e−01
D_m	Diffusion coeff. of MMPs	−2.9334e−01	−9.5195e−02	−2.8800e+01	−1.6365e+02
χ_D	Haptotaxis coeff. of DCCs	+8.9096e−01	−3.4507e−01	−1.3500e+01	−3.1985e+00
χ_S	Haptotaxis coeff. of CSCs	−9.4425e−03	−3.5106e−03	+1.5600e+00	+4.9956e−01
χ_F	Haptotaxis coeff. of fibroblasts	−7.0482e−03	−8.6437e−04	±0	−1.6845e−03
λ^{D}	EGF receptors per DCC	−3.2691e−02	+4.6710e−02	+5.4000e−01	+7.5617e−01
λ^{S}	EGF receptors per CSC	+5.1239e−04	−6.5509e−04	±0	−1.4768e−02
k_D	EGF unbinding/binding	+5.1703e−02	−7.4019e−02	−8.6400e−01	−1.1744e+00
Γ	Average of total EGF	−2.1830e−01	+3.1164e−01	+3.6000e+00	+5.0090e+00
μ_0	EMT factor	−6.6859e−02	+9.5767e−02	+1.1345e+00	+1.5432e+00
$\mu_{1/2}$	Critical EGF density	+1.7618e−02	−2.5178e−02	−2.8800e−01	−4.0878e−01
μ_D	Proliferation rate of DCCs	+2.3304e−01	+3.9116e−02	+1.2000e−01	−6.8597e−04
μ_S	Proliferation rate of CSCs	+2.2971e−04	+4.9220e−02	±0	+4.6599e−03
μ_F	Proliferation rate of fibroblasts	−1.3865e−04	−5.2592e−05	±0	+1.1644e−03
μ_v	ECM remodelling rate	+5.2516e−02	+1.0917e−02	+6.6000e−01	+2.4808e−01
β_F	Apoptosis of fibroblasts	+1.2117e−03	+4.8903e−04	±0	−7.7809e−03
β_m	Decay rate of MMPs	−4.7396e−02	−9.1276e−03	−4.9200e−01	−8.6865e−01
α_D	MMP production rate of DCCs	+3.6965e−01	+2.6936e−02	±0	+7.9042e−01
α_S	MMP production rate of CSCs	+6.4883e−03	+6.6901e−03	+6.6000e−01	+1.3518e−01
δ_v	ECM degradation rate	−6.8955e−06	−4.4457e−06	±0	−4.8110e−05
μ_{TRA}	Transdifferentiation rate	−2.0113e−01	−6.7081e−01	−1.2000e+01	−3.6641e+01

A large absolute value in the table indicates a high influence of the parameter (rows) on the corresponding attribute (column). For details on the computation see Sect. 3.2, the results are discussed in Sect. 4

for the front distance mean that no influence on the relative invasion speed could be measured in the simulation. For a discussion of the results of the parameter study, we refer to the following section.

4 Experiments and Discussion

The initial conditions that we use in the one-dimensional case are:

$$c_0^{\mathrm{D}}(x) = \exp(-20\,x^2), \quad c_0^{\mathrm{S}}(x) = c_0^{\mathrm{F}}(x) = 0, \quad v_0(x) = 1 - 0.5\,c_0^{\mathrm{D}}(x), \\ m_0(x) = 0.2\,c_0^{\mathrm{D}}(x), \tag{26}$$

for all $x \in \Omega$, whereas in the two-dimensional case:

$$c_0^{\mathrm{D}}(\mathbf{x}) = \begin{cases} \sin\left(5\,\arctan\left(\frac{x_2}{x_1}\right)\right), & \text{if } x_1^2 + x_2^2 < 4,\ x_2 \le 0,\ x_1 \ge 0, \\ \sin\left(5\,\left(\pi + \arctan\left(\frac{x_2}{x_1}\right)\right)\right), & \text{if } x_1^2 + x_2^2 < 4,\ x_2 \le 0,\ x_1 < 0, \\ 0, & \text{otherwise}, \end{cases} \tag{27}$$

$$c_0^{\mathrm{S}}(\mathbf{x}) = c_0^{\mathrm{F}}(\mathbf{x}) = 0,\ v_0(\mathbf{x}) = 1 - c_0^{\mathrm{D}}(\mathbf{x}),\ m_0(\mathbf{x}) = \frac{1}{20}\,c_0^{\mathrm{D}}(\mathbf{x}), \quad \mathbf{x} = (x_1, x_2) \in \Omega. \tag{28}$$

We use a fine computational grid with 7000 cells in the one-dimensional cases and 250×250 for the two-dimensional simulations. Further details on the various experimental settings are given in Appendix.

Figure 2 presents the numerical solution of the system (17) over a one-dimensional domain with ICs (26) and parameters taken from the Table 1. In the initial conditions no CSCs are included, they are formed by the DCCs after undergoing EMT. The CSCs exhibit higher motility and invasiveness than the DCCs; they escape the main body of the tumour and invade the ECM while developing highly dynamic phenomena like the merging and emerging of concentrations. In a similar way, Fig. 3 presents the dynamics of the same model (17) and parameters on a two-dimensional domain. We see, in particular, laterally propagating waves in the migration of the CSCs, which are due to the non-convexity of the DCC front in the initial conditions. These dynamics do not dissipate with time; see e.g. the experiments presented in Figs. 5, 6, as well as in other cancer invasion models (e.g. Andasari et al. 2011; Chaplain and Lolas 2005; Kolbe et al. 2016). This might be a consequence of the absence of a "dying" term in the model that reflects the well-known property of immortality of cancer cells.

In Fig. 4, we compare three different types of ECM remodelling: The case without matrix remodelling (Experiment IIa) is used for comparison reasons. The matrix is depleted by the MMPs, which are produced by the cancer cells, creating "holes" in which the cells cannot attach and translocate. The case of self-remodelling is included as it is one of the most prominent in the literature. We see the stronger confinement of both types of cancer cells and the "sharper" ECM. In the cancer-associated fibroblast remodelling case, we notice the faster invasion of the CSCs, as well as repair of the ECM by the fibroblast cells.

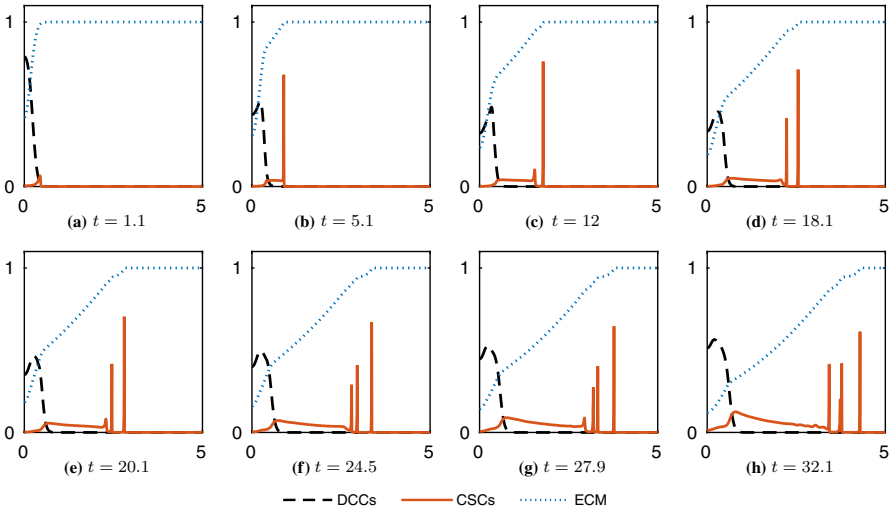

Fig. 2 Time evolution of the one-dimensional cancer invasion system (17). **a** The CSCs are produced from the DCCs via the EMT, **b**, **c** due to their higher motility, the CSCs escape the main body of the tumour and invade the ECM faster than the DCCs. Two distinct propagating fronts have been formed, **d**–**f** the CSCs present dynamic travelling merging and emerging concentrations; the DCCs propagate into the ECM slower. The computational setting is described in Experiment Ia in Appendix

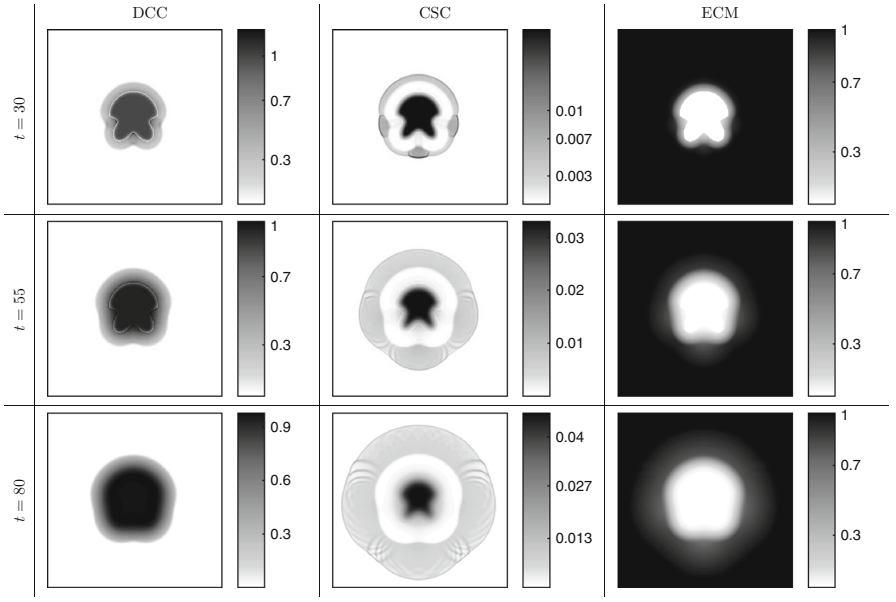

Fig. 3 Time evolution of the two-dimensional cancer invasion system (17), in Experiment IIIa. Similar to the one-dimensional case (Fig. 2), the invasion of the DCCs onto the ECM is smooth and mostly driven by proliferation and diffusion. The CSCs exhibit richer dynamics and patterns in their invasion. In particular, laterally propagating and interacting waves appear due to the non-convexity of the front of the initial concentrations. The ECM is depleted by the MMPs which in turn are produced by the cancer cells and is constantly remodelled by the fibroblast cells. An initially uniform distribution of the ECM is assumed

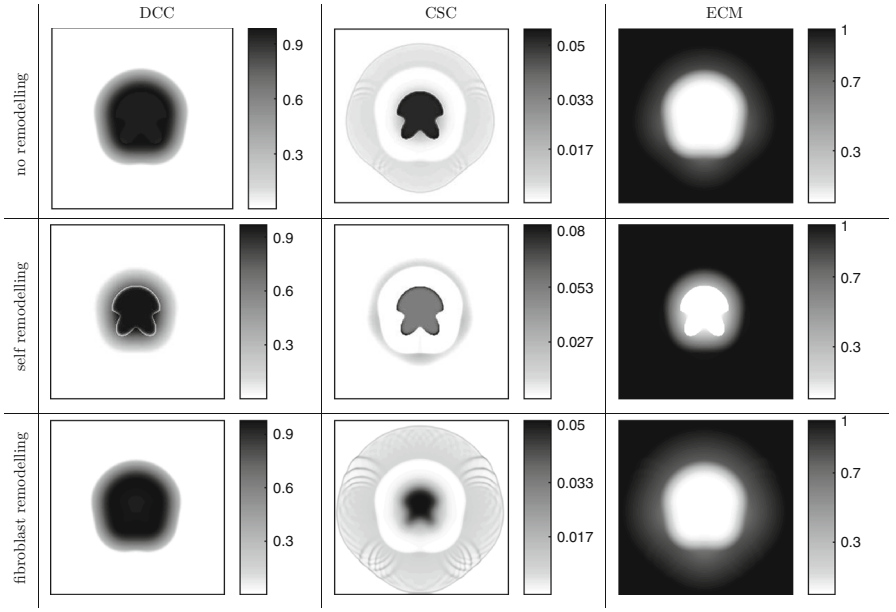

Fig. 4 Comparison between three different types of ECM remodelling at time $t = 90$. (*Upper row*, Experiment IIIb) The ECM is depleted by the MMPs and is not remodelled. Newly sprout CSCs in the kernel of the tumour are unable to adhere and escape the main body of the tumour. This case is used for comparison reasons. (*Middle row*, Experiment IIIc) The ECM is automatically recovered as long as there is some pre-existing ECM. A non-uniform ECM is remodelled by filling the free volume leading to a uniform ECM distribution. (*Lower row*, Experiment IIIa) The matrix is remodelled by fibroblast cells that are haptotactically directed towards lower densities of the ECM. This recovers the matrix in the kernel of the tumour allowing for the CSCs to adhere and escape the tumour

In Fig. 5, we compare different EMT models: a typical constant EMT rate μ_{EMT} in (17) and our EGF-driven μ_{EMT} coefficient proposed in (13). For the one-dimensional case, we start this comparison with parameters in Table 1 (modified to fit the one-dimensional case), and subsequently adjusted them so that the invasiveness (propagating front of the CSCs and DCCs) and distributions of the cancer cells coincide at different time instances for the constant rate and the EGF-driven EMT, see Fig. 5 upper and middle rows. In the lower row, we consider the EGF-driven EMT and the pathological situation, where the total amount of EGF given by Γ in (10) is extremely low (of the order of 10^{-3}). As expected, only a small amount of DCCs have undergone EMT, leading to a small but still existent number of CSCs which invade the ECM.

In Fig. 6, we go one step further and first consider the same coefficients as the ones that give the coincidence between the constant rate and the EGF-driven EMT, see Fig. 5. We consider a small initial tumour (with a maximum density of 10^{-3}) and simulate the evolution of the cancer dynamics without translocation terms. We see that in the constant rate EMT case, the CSCs quickly rise and achieve densities comparable to the DCCs'. This means that the metastatic part of the tumour would be as detectable as its main body. In contrast, in the EGF-driven EMT case, we observe that the density of the CSCs remains low (negligible relatively to the DCCs for a

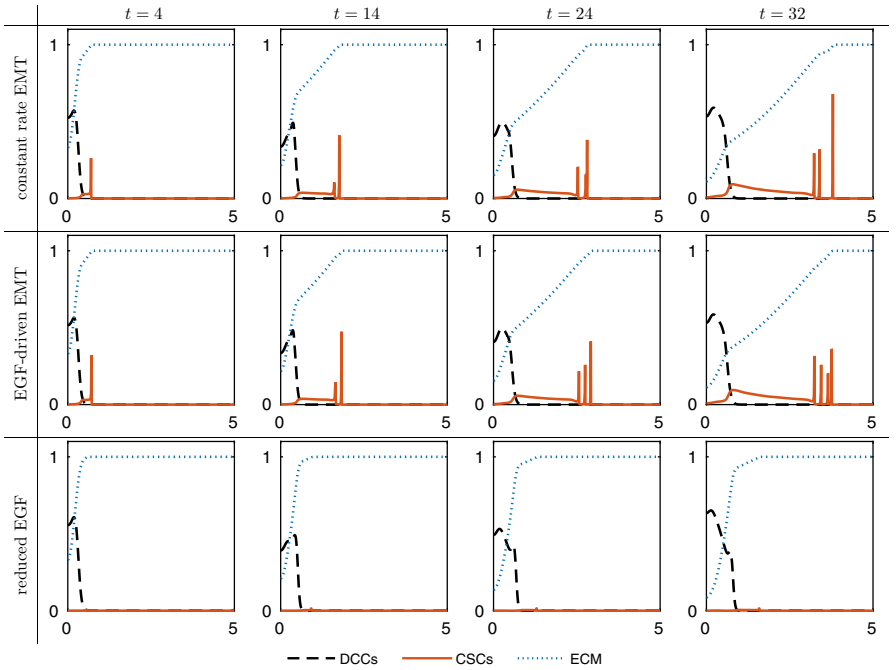

Fig. 5 Comparison between the constant rate EMT (*upper row*, Experiment IIa), versus the EGF-driven EMT, i.e. μ_{EMT} given by (13) (*middle* and *lower rows*, Experiments Ib, Ic). The parameters in the upper and middle graph are based on the Table 1 and are adjusted so that the invasiveness of the CSCs and the DCCs coincide. We observe that the components of the solution are qualitatively the same; there is a difference in the number of peaks that the CSCs exhibit. In the third row, we present a particular experiment of the EGF-driven EMT case, where the total EGF has been depleted to a low value (10^{-3}). A single propagating low-density peak of CSCs appears, demonstrating the adjustability of our model to the pathological situation of very low EGF density

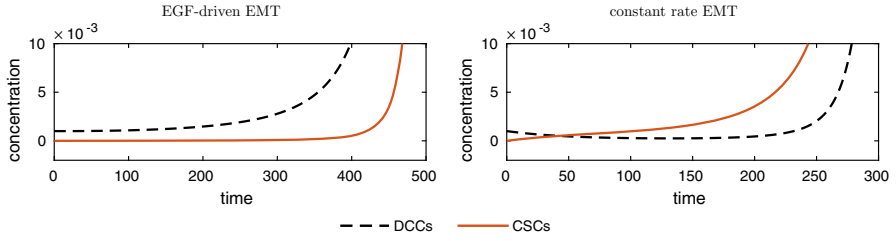

Fig. 6 Comparison of the EGF-driven EMT (*left*, Experiment Id) with the constant rate EMT (*right*, Experiment IIb) in terms of the production of CSCs. We use the same parameters as shown in Fig. 5 with an initial DCC concentration of a maximum value 10^{-3}. We can see that in the EGF-driven EMT case, there is no concentration of the CSCs comparable to the one of the DCCs until the DCC concentration has increased considerably. Loosely translated, our model predicts that small tumours produce CSCs that cannot be detected due to their low densities. On the other hand, in the constant rate EMT case, the density of the CSCs raises quickly to become comparable to the DCCs level and can be easily detected

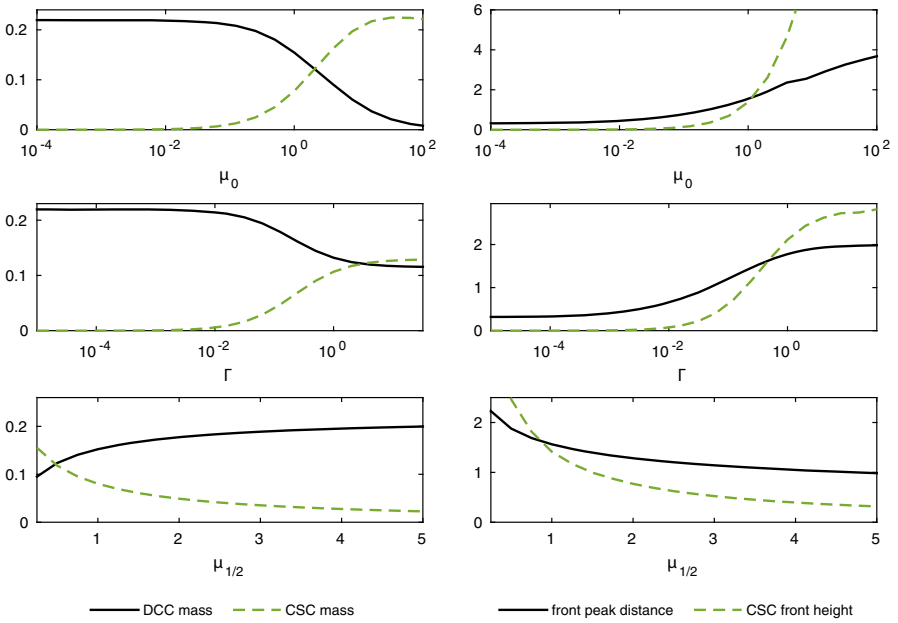

Fig. 7 Influence of the parameters $\mu_0, \Gamma, \mu_{1/2}$ on the mass and the invasiveness of the cancer cells. (*Upper row*) High values of the maximum EMT rate μ_0 in (3) promote the CSCs and deplete the DCCs (*left*). The front distance between the two families of cancer cells and the density of the CSCs at the propagating front increases (*right*). (*Middle row*) When the (average) concentration of EGF Γ, cf. (10), increases, the masses of the two cancer cell types are driven to a stable situation (*left*). Similarly, their relative invasiveness and the density of the CSCs indicate stagnation (*right*). (*Lower row*) The increase in $\mu_{1/2}$ in (3) is beneficial for the DCCs. It depletes the CSCs and decreases the density and the distance of the propagating fronts; in effect, it weakens the migration and growth of CSCs. This graph suggests that enhancing $\mu_{1/2}$ prevents the migration of the CSCs, cf. Experiment Ia

long time), but start to increase later. But even in the initial phase, a few CSCs are present (relative number at $t = 400$ or so) and thus can invade the ECM. Our model hence is able to produce a scenario where metastatic CSCs can be produced also by "small" tumours and remain un-detectable in comparison with the main body of the DCCs.

Regarding the sensitivity of the model simulation as shown Table 3, cf. Sect. 3.2, we can see that the invasiveness of the CSCs relative to the DCCs (quantified by the front-peak distance) is not only affected by the haptotactic sensitivity of both types of cancer cells, but also by the EGF. Indeed, an increase in the total amount of EGF or in the EMT strength has a significant positive impact, while a higher rate of fibroblast transdifferentiation would weaken the aggressiveness. Further, higher ECM remodelling rates increase the tumour by increasing the mass of both cancer types, the invasiveness of the CS, and also in the density of the invading CSCs (i.e. the CSC front height), see Fig. 4 (compare bottom and top row). The apoptosis of fibroblasts moreover supports the tumour while having a stronger influence on the DCCs than on the CSCs. In comparison with the transdifferentiation, which weakens the tumour growth overall, the proliferation of the fibroblasts has only a weak negative impact on the tumour size. An increase in the number of EGF receptors on the DCCs would

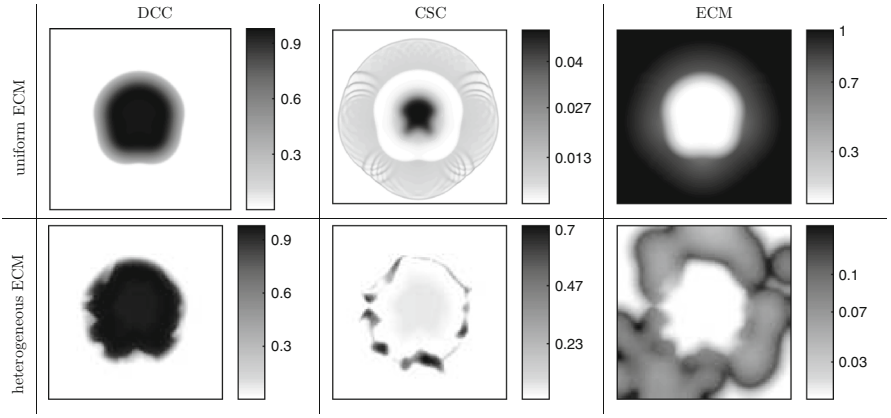

Fig. 8 Comparison of two invasion systems with uniform and non-uniform ECM, respectively. System (17) is resolved with uniform initial ECM distribution (*upper row*, Experiment IIIa), and with non-uniform initial distribution of the ECM (*lower row*, cf. Experiment IVa). In both cases, the ECM is degraded by the MMPs and remodelled by the fibroblast cells. We observe a significant loss of symmetry in the invasion of the CSCs with the higher concentrations following the structure of the ECM

promote the EMT transition and thus the mass and the invasiveness of the DCCs. On the other hand, increasing the receptors on the CSCs has the inverse but significantly weaker effect.

In Fig. 7, we can see the effect that the EMT-controlling parameters μ_0, Γ, $\mu_{1/2}$ have on the mass and on the primary propagating front of the DCCs and the CSCs. In particular, we observe that the increase in μ_0 (maximum EMT rate) causes the depletion of the DCCs. Moreover, an increase in Γ (average EGF concentration in the environment) increases the amount of CSCs relative to DCCs, until an eventual stagnation of the CSCs aggressiveness, with no change upon further increase in Γ. Higher values of the constant $\mu_{1/2}$ have a somewhat different effect: The aggressiveness of CSCs (in both density and speed) decays as is their total mass. Hence, increasing $\mu_{1/2}$ or decreasing μ_0 and Γ would have a beneficial impact to the patient in our model.

With our parameter investigations, we have identified potential treatments that affect the invasiveness and migration of the CSCs. Our model faithfully predicts that decreasing the total amount of EGF in the environment, or the maximum EMT rate μ_0, or the amount of EGFRs λ^{D}, or increasing $\mu_{1/2}$, leads to a direct decrease in the EMT rate μ_{EMT} as one would expect based on the setting for the model. Furthermore, the dependence of the mass of CSCs and DDCs on the effective EMT rate agrees with the expectations. But not only the height of the CSC front-peak, but also the difference between the position of the peaks of the two cell populations is positively correlated with the effective EMT rate and thus with the CSC mass. Similar results can be obtained by the inhibition of the remodelling of the ECM, or by the enhancement of transdifferentiation, and by the prevention of fibroblast apoptosis.

In Fig. 8, we can see the effect that an initially non-uniform ECM has on the migration of the cancer. We note, in particular, that the invasion is no longer uniform

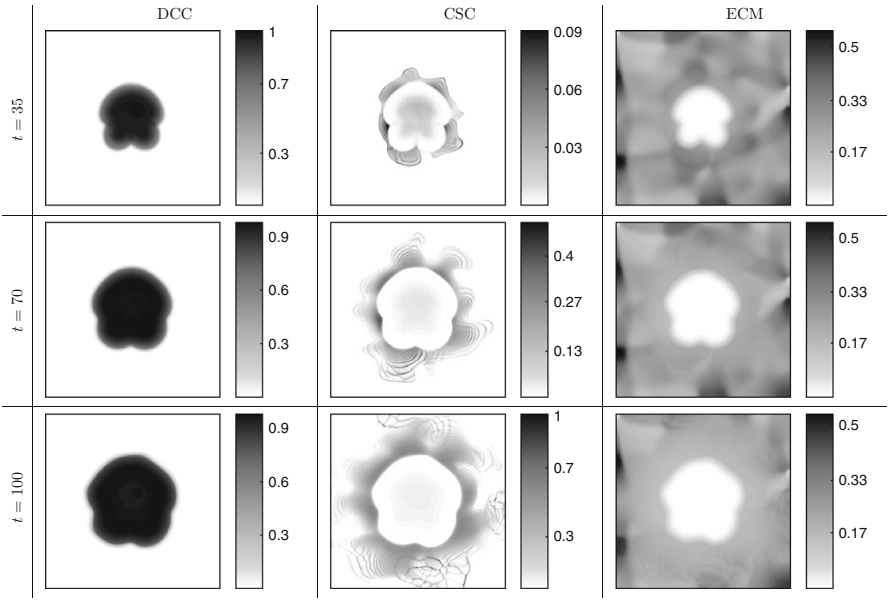

Fig. 9 Invasion of the ECM (*right*) by the DCCs (*left*) and CSCs (*center*) including all the components of the model: The ECM is assumed to be non-uniform and remodelled by the fibroblast cell, the EMT is EGF-driven, and the proliferation is modelled by the positive-part logistic function. Note the wavy pattern due to the CSCs migration of the ECM, Experiment IVb

and it is highly influenced by the gradients of the ECM. These can lead to the creation of islands/clusters of CSCs.

In Fig. 9, we present the invasion of the ECM by the cancer cells using the full system (17) and parameters as shown in Table 1. We note that in the invasion of the CSCs, nonlinear waves appear that are created by the interaction of their propagating fronts.

5 Conclusion

The main goal of this work was to develop a mathematical model and get a deeper insight into the role of EMT in the invasion of cancer. In particular, we integrate the EGF-driven-EMT process and develop an algebraic-elliptic model (8) to account for the amount of EGF molecules in the vicinity of a tumour. To this end, we introduce a non-constant EMT coefficient (13) that drives the de-differentiation of DCCs to CSCs.

This EMT model is combined with a haptotaxis system of the Keller-Segel type that models the invasion of the ECM by both DCCs and CSCs. We endow the resulting system with a term describing the degradation of the ECM by matrix degenerating MMPs secreted by both families of cancer cells, and by the ECM remodelling driven by cancer-associated fibroblast cells (16). The fibroblast cells are assumed to be produced by the CSCs via a cell transdifferentiation program (15). Another particular component of the proposed model is the positive-part logistic proliferation term. Numerically, we

resolve the full system in one- and two-spatial dimensions with a robust higher-order implicit–explicit finite volume scheme developed in our previous works (Kolbe et al. 2016; Hellmann et al. 2016).

With our numerical experiments, we are able to reproduce qualitatively the detachment of CSCs from the main tumour body with time after onset of the EMT. This detachment is one of the first steps in metastasis for which the CSCs are considered responsible (Brabletz et al. 2005; Katsumo et al. 2013; Kong et al. 2011; Jordan et al. 2006). The detachment is a consequence of the enhanced motitilty of the CSCs compared to the DCCs, a property acquired due to the process of EMT. The spatial distribution of the CSCs is modulated by the density of the ECM, to which the cells adhere, and which is degraded by the cells. The inclusion of fibroblast-dependent remodelling of the ECM leads to smoother and thus more realistic profiles of the ECM density. The inclusion of a rate of EMT which depends on EGFR activation and thus on EGF concentration further improves the model since by this the regulation of CSCs by modulation of EMT, e.g. by adding EGFR inhibitors as observed in biological experiments (Mendelsohn and Baselga 2000; Voon et al. 2013) is now included. However, the inherent property of the model, which produces highly dynamic emerging and merging CSC concentration peaks is not altered by the newly included processes.

We are moreover able to deduce information regarding the invasiveness of CSCs. Using the components of the EMT subsystem, we can suggest potential scenarios for their control. In particular, performing a sensitivity analysis on the parameters of the models to verify that the parameters and components of the EMT are among the most influential in the invasiveness and aggressiveness of the tumour. With our study, we can see that the CSCs produced by small tumours become detectable only in later stages of the evolution of the cancer, while in the meantime, they migrate in a fast pace.

Appendix

Experiment Description

Here, we give technical details on the experiments that have been presented in this work. Our one-dimensional simulations have been computed on the domain $\Omega = [0, 7.5]$ with the initial conditions (26), and the experiments in two dimensions have been conducted on $\Omega = [-5, 5]^2$ with the initial data (27), (28). Wherever not otherwise stated, we have employed the parameters from Table 1.

The space and time domains are chosen such that we avoid interference on the wave propagation by the boundary conditions.

Experiment Ia One-dimensional, EGF-driven EMT With parameters from Table 1 except for $\mu_0 = 0.55,\ k_D = 0.5,\ \Gamma = 7.5^{-1}$. See also Figs. 2 and 7. The convergence study (see Table 2) and the sensitivity analysis, see Table 3, have been conducted on a smaller domain $\Omega_S = [0, 3]$.

Experiment Ib One-dimensional, adjusted EMT The parameters have been adjusted, so that the invasiveness of the CSCs coincides with the Experiment IIa: $\mu_0 = 0.034,\ \mu_{1/2} = 0.4,\ k_D = 0.2,\ \lambda^D = 3,\ \Gamma = 7.5^{-1}$. See also Fig. 5 (middle row).

Experiment Ic One-dimensional, adjusted EMT & low EGF Same as Experiment Ib, with low EGF concentration: $\mu_0 = 0.034,\ \mu_{1/2} = 0.4,\ k_D = 0.2,\ \lambda^D = 3,\ \Gamma = 10^{-3}$. See also Fig. 5 (lower row).

Experiment Id Adjusted EMT & low initial DCC concentration Same parameters as in Experiment Ib. Advection and diffusion terms were neglected. The initial conditions $c_0^D = 10^{-3},\ c_0^S = 0,\ c_0^F = 0,\ v_0 = 1,\ m_0 = 10^{-6}$ have been employed. See also Fig. 6 (left).

Experiment IIa One-dimensional, constant EMT rate Our EMT model from Sect. 2.2 has been neglected, and the EMT transition coefficient in system (17) has been taken as a constant: $\mu_{\text{EMT}} = 0.017$. The invasiveness of the CSCs coincides with Experiment Ib. See Fig. 5 (upper row).

Experiment IIb Constant EMT rate & low initial DCC concentration Same parameters as in Experiment IIa. Advection and diffusion terms were neglected. The initial conditions $c_0^D = 10^{-3},\ c_0^S = 0,\ c_0^F = 0,\ v_0 = 1,\ m_0 = 10^{-6}$, have been employed as in Experiment Id. See also Fig. 6 (right).

Experiment IIIa Two-dimensional, uniform ECM & fibroblast remodelling Parameters from Table 1. See Figs. 3 and 4 (lower row).

Experiment IIIb Two-dimensional, uniform ECM & no remodelling Same as Experiment IIIa, without matrix remodelling: $\mu_v = 0$. See Fig. 4 (upper row).

Experiment IIIc Two-dimensional, uniform ECM & self-remodelling Same as Experiment IIIa, with self-remodelling, i.e. the term $+\mu_v\, c^{\mathrm{F}}\,(1 - c^{\mathrm{D}} - c^{\mathrm{S}} - c^{\mathrm{F}} - v)^+$ for the ECM in system (17) has been replaced by $+\mu_v\, v\,(1 - c^{\mathrm{D}} - c^{\mathrm{S}} - c^{\mathrm{F}} - v)^+$, hence the fibroblasts have been neglected. See Fig. 4 (middle row).

Experiment IIId Two-dimensional, uniform ECM & fibroblast remodelling & smooth initial data Same as Experiment IIIa with smooth initial data for the convergence study, see Table 2:

$$c_0^{\mathrm{D}}(\mathbf{x}) = \exp(-\|\mathbf{x}\|_2^2),\ c_0^{\mathrm{S}}(\mathbf{x}) = c_0^{\mathrm{F}}(\mathbf{x}) = 0,\ v_0(\mathbf{x}) = 1 - c_0^{\mathrm{D}}(\mathbf{x}),\ m_0(\mathbf{x}) = \frac{1}{20}\, c_0^{\mathrm{D}}(\mathbf{x}), \quad \mathbf{x} = (x_1, x_2) \in \Omega.$$

Experiment IVa Two-dimensional, non-uniform ECM Same as Experiment IIIa with an ECM initial concentration v_0 different from (28). The non-uniform initial ECM v_0 has been constructed by a random distribution of fibroblast cell concentrations acting without other influences on the domain. We have conducted the simulation on a 100×100 computational grid (lower resolution as opposed to the other experiments). See Fig. 8 lower row.

Experiment IVb Two-dimensional, non-uniform ECM Similar to Experiment IVa, the non-uniform initial ECM v_0 has been constructed by a random distribution of fibroblast cell concentrations acting on the domain. As a result the initial ECM concentration is different from the case in Experiment IVa. We have conducted the simulation using the standard grid resolution with 250×250 mesh cells. See also Fig. 9.

References

Alt W, Lauffenburger DA (1987) Transient behavior of a chemotaxis system modelling certain types of tissue inflammation. J Math Biol 24(6):691–722

Andasari V, Gerisch A, Lolas G, South AP, Chaplain MAJ (2011) Mathematical modelling of cancer cell invasion of tissue: biological insight from mathematical analysis and computational simulation. J Math Biol 63(1):141–171

Anderson ARA, Chaplain MAJ, Newman EL, Steele RJC, Thompson AM (2000) Mathematical modelling of tumour invasion and metastasis. Comput Math Methods Med 2(2):129–154

Armitage P, Doll R (1954) The age distribution of cancer and a multi-stage theory of carcinogenesis. Br J Cancer 8(1):1

Bellomo N, Li NK, Maini PK (2008) On the foundations of cancer modelling: selected topics, speculations, and perspectives. Math Models Methods Appl Sci 18(04):593–646

Brabletz T, Jung A, Spaderna S, Hlubek F, Kirchner T (2005) Opinion: migrating cancer stem cells—an integrated concept of malignant tumour progression. Nat Rev Cancer 5(9):744–749

Bray D (2001) Cell movements: from molecules to motility. Garland Science, New York

Chaplain MAJ, Lolas G (2005) Mathematical modelling of cancer cell invasion of tissue. The role of the urokinase plasminogen activation system. Math Models Methods Appl Sci 15(11):1685–1734

Cox TR, Erler JT (2011) Remodeling and homeostasis of the extracellular matrix: implications for fibrotic diseases and cancer. Dis Models Mech 4(2):165–178

Domschke P, Trucu D, Gerisch A, Chaplain MAJ (2014) Mathematical modelling of cancer invasion: implications of cell adhesion variability for tumour infiltrative growth patterns. J Theor Biol 361:41–60

Eladdadi A, Isaacson D (2008) A mathematical model for the effects of HER2 overexpression on cell proliferation in breast cancer. Bull Math Biol 70:1707–1729

Erler JT, Weaver VW (2009) Three-dimensional context regulation of metastasis. Clin Exp Metastasis 26(1):35–49

Fan YL, Zheng M, Tang YL, Liang XH (2013) A new perspective of vasculogenic mimicry: EMT and cancer stem cells (review). Oncol Lett 6(5):1174–1180

Fisher JC (1958) Multiple-mutation theory of carcinogenesis. Nature 181(4609):651–652

Ganguly R, Puri IK (2006) Mathematical model for the cancer stem cell hypothesis. Cell Proliferat 39(1):3–14

Gao D, Vahdat LT, Wong S, Chang JC, Mittal V (2012) Microenvironmental regulation of epithelial–mesenchymal transitions in cancer. Cancer Res 72(19):4883–4889

Gerisch A, Chaplain MAJ (2006) Robust numerical methods for taxis-diffusion-reaction systems: applications to biomedical problems. Math Comput Model 43(1):49–75

Gerisch A, Chaplain MAJ (2008) Mathematical modelling of cancer cell invasion of tissue: local and nonlocal models and the effect of adhesion. J Theor Biol 250(4):684–704

Gupta PB, Chaffer CL, Weinberg RA (2009) Cancer stem cells: mirage or reality? Nat Med 15(9):1010–1012

Hellmann N, Kolbe N, Sfakianakis N (2016) A mathematical insight in the epithelial–mesenchymal-like transition in cancer cells and its effect in the invasion of the extracellular matrix. Bull Braz Math Soc 47(1):397–412

Hillen T, Painter K (2012) Transport models for movement in oriented habitats and anisotropic diffusion. In: Petrovskii S, Lewis MA, Maini P (eds) Dispersal, individual movement and spatial ecology: a mathematical perspective. Springer, Heidelberg

Hillen T, Painter K (2013) Mathematical modelling of glioma growth: the use of diffusion tensor imaging (dti) data to predict the anisotropic pathways of cancer invasion. J Theor Biol 323:25–39

Hundsdorfer W, Verwer JG (2003) Numerical solution of time-dependent advection-diffusion-reaction equations, vol 33. Springer, Heidelberg

Imai Y, Leung CKH, Friesen HG, Shiu RPC (1982) Epidermal growth factor receptors and effect of epidermal growth factor on growth of human breast cancer cells in long-term tissue culture. Cancer Res 42(11):4394–4398

Jeulin C, Seltzer V, Bailbé D, Andreau DK, Marano F (2008) EGF mediates calcium-activated chloride channel activation in the human bronchial epithelial cell line 16HBE14o-: involvement of tyrosine kinase p60c-src. Am J Physiol Lung Cell Mol Physiol 295(3):L489–L496

Johnston MD, Maini PK, Jonathan-Chapman S, Edwards CM, Bodmer WF (2010) On the proportion of cancer stem cells in a tumour. J Theor Biol 266(4):708–711

Jordan CT, Guzman M, Noble ML (2006) Cancer stem cells. N Engl J Med 355:1253–1261

Kaplan RN, Riba RD, Zacharoulis S, Bramley AH, Vincent L, Costa C, MacDonald DD, Jin DK, Shido K, Kerns SA, Zhu Z, Hicklin D, Wu Y, Port JL, Altorki N, Port ER, Ruggero D, Shmelkov SV, Jensen KK, Rafii S, Lyden D (2005) VEGFR1-positive haematopoietic bone marrow progenitors initiate the pre-metastatic niche. Nature 438(7069):820–827

Katsumo Y, Lamouille S, Derynck R (2013) TGF-β signaling and epithelial–mesenchymal transition in cancer progression. Curr Opin Oncol 25(1):76–84

Kawamoto T, Mendelsohn J, Le A, Sato GH, Lazar CS, Gill GN (1984) Relation of epidermal growth factor receptor concentration to growth of human epidermoid carcinoma A431 cells. J Biol Chem 259(12):7761–7766

Keller EF, Segel LA (1970) Initiation of slime mold aggregation viewed as an instability. J Theor Biol 26(3):399–415

Kennedy CA, Carpenter MH (2003) Additive Runge–Kutta schemes for convection-diffusion-reaction equations. Appl Numer Math 1(44):139–181

Kim DH, Han K, Gupta K, Kwon KW, Suh KY, Levchenko A (2009) Mechanosensitivity of fibroblast cell shape and movement to anisotropic substratum topography gradients. Biomaterials 30(29):5433–5444

Kim Y, Friedmann A (2010) Interaction of tumor with its micro-environment: a mathematical model. Bull Math Biol 72(5):1029–1068

Klein P, Mattoon D, Lemmon MA, Schlessinger J (2004) A structure-based model for ligand binding and dimerization of EGF receptors. Proc Natl Acad Sci USA 101(4):929–934

Kolbe N, Kat'uchová J, Sfakianakis N, Hellmann N, Lukáčová-Medvid'ová M (2016) A study on time discretization and adaptive mesh refinement methods for the simulation of cancer invasion : the urokinase model. Appl Math Comput 273:353–376

Kong D, Li Y, Wang Z, Sarkar FH (2011) Cancer stem cells and epithelial-to-mesenchymal transition (emt)-phenotypic cells: are they cousins or twins? Cancers 3:716–729

Kurganov A, Lukáčová-Medvid'ová M (2014) Numerical study of two-species chemotaxis models. Discrete Continuous Dyn Syst Ser B 19(1):131–152

Mani SA, Guo W, Liao MJ, Eaton EN, Ayyanan A, Zhou AY, Brooks M, Reinhard F, Zhang CC, Shipitsin M, Campbell LL, Polyak K, Brisken C, Yang J, Weinberg RA (2008) The epithelial–mesenchymal transition generates cells with properties of stem cells. Cell 133(4):704–715

McDougall SR, Anderson ARA, Chaplain MAJ, Sheratt JA (2002) Mathematical modelling of flow through vascular networks: implications for tumour-induced angiogenesis and chemotherapy strategies. Bull Math Biol 64(4):673–702

Mendelsohn J, Baselga J (2000) The egf receptor family as targets for cancer therapy. Oncogene 19:6550–6555

Michor F (2008) Mathematical models of cancer stem cells. J Clin Oncol 26(17):2854–2861

Neagu A, Mironov V, Kosztin I, Barz B, Neagu M, Moreno-Rodriguez RA, Markwald RR, Forgacs G (2010) Computational modelling of epithelial–mesenchymal transformations. Biosystems 100(1):23–30

Nordling CO (1953) A new theory on the cancer-inducing mechanism. Br J Cancer 7(1):68

Özcan F, Klein P, Lemmon MA, Lax I, Schlessinger J (2006) On the nature of low- and high-affinity EGF receptors on living cells. Proc Natl Acad Sci USA 103(15):5735–5740

Pareschi L, Russo G (2005) Implicit–explicit Runge–Kutta schemes and applications to hyperbolic systems with relaxation. J Sci Comput 25(1–2):129–155

Perumpanani AJ, Sherratt JA, Norbury J, Byrne HM (1996) Biological inferences from a mathematical model for malignant invasion. Invasion Metastasis 16(4–5):209–221

Preziosi L (2003) Cancer modelling and simulation. CRC Press, Boca Raton

Radisky DC (2005) Epithelial–mesenchymal transition. J Cell Sci 118(19):4325–4326

Reya T, Morrison SJ, Clarke MF, Weissman IL (2001) Stem cells, cancer, and cancer stem cells. Nature 414(6859):105–111

Robbins KC, Summaria L, Elwyn D, Barlow GH (1965) Further studies on the purification and characterization of human plasminogen and plasmin. J Biol Chem 240(1):541–550

Sasaki T, Hiroki K, Yamashita Y (2013) The role of epidermal growth factor receptor in cancer metastasis and microenvironment. Biomed Res Int 2013:546318. doi:10.1155/2013/546318

Shien K, Toyooka S, Yamamoto H, Soh J, Jida M, Thu KL, Hashida S, Makl Y, Ichlhara E, Asano H, Tsukuda K, Taglkawa N, Klura K, Gazdar AF, Lam WL, Miyoshil S (2013) Acquired resistance to EGFR inhibitors is associated with a manifestation of stem cell-like properties in cancer cells. Cancer Res 73(10):3051–3061

Stiehl T, Marciniak-Czochra A (2012) Mathematical modeling of leukemogenesis and cancer stem cell dynamics. Math Model Nat Phenom 7(01):166–202

Stinner C, Surulescu C, Uatay A (2015) Global existence for a go-or-grow multiscale model for tumor invasion with therapy. Preprint on webpage at http://nbn-resolving.de/urn/resolver.pl?urn:nbn:de:hbz:386-kluedo-42943

Stokes CL, Lauffenburger DA (1991) Analysis of the roles of microvessel endothelial cell random motility and chemotaxis in angiogenesis. J Theor Biol 152(3):377–403

Stokes CL, Lauffenburger DA, Williams SK (1991) Migration of individual microvessel endothelial cells: stochastic model and parameter measurement. J Cell Sci 99(2):419–430

Thiery JP (2002) Epithelial–mesenchymal transitions in tumour progression. Nat Rev Cancer 2(6):442–454

Vainstein V, Kirnasovsky OU, Kogan Y, Agur Z (2012) Strategies for cancer stem cell elimination: insights from mathematical modelling. J Theor Biol 298:32–41

Van Leer B (1977) Towards the ultimate conservative difference scheme. IV. A new approach to numerical convection. J Comput Phys 23(3):276–299

Voon DC, Wang H, Koo JKW, Chai JH, Hor YT, Tan TZ, Chu YS, Mori S, Ito Y (2013) EMT-induced stemness and tumorigenicity are fueled by the EGFR/Ras pathway. PLoS ONE 8(8):e70427

Zhu X, Zhou X, Lewis MT, Xia L, Wong S (2011) Cancer stem cell, niche and EGFR decide tumor development and treatment response: a bio-computational simulation study. J Theor Biol 269(1):138–149